Simultaneous Mapping of Water Shift and B_1 (WASABI)—Application to Field-Inhomogeneity Correction of CEST MRI Data

Patrick Schuenke,[1]* Johannes Windschuh,[1] Volkert Roeloffs,[2] Mark E. Ladd,[1] Peter Bachert,[1] and Moritz Zaiss[1]

Purpose: Together with the development of MRI contrasts that are inherently small in their magnitude, increased magnetic field accuracy is also required. Hence, mapping of the static magnetic field (B_0) and the excitation field (B_1) is not only important to feedback shim algorithms, but also for post-process contrast-correction procedures.

Methods: A novel field-inhomogeneity mapping method is presented that allows simultaneous mapping of the water shift and B_1 (WASABI) using an off-resonant rectangular preparation pulse. The induced Rabi oscillations lead to a sinc-like spectrum in the frequency-offset dimension and allow for determination of B_0 by its symmetry axis and of B_1 by its oscillation frequency.

Results: Stability of the WASABI method with regard to the influences of T_1, T_2, magnetization transfer, and repetition time was investigated and its convergence interval was verified. B_0 and B_1 maps obtained simultaneously by means of WASABI in the human brain at 3 T and 7 T can compete well with maps obtained by standard methods. Finally, the method was applied successfully for B_0 and B_1 correction of chemical exchange saturation transfer MRI (CEST-MRI) data of the human brain.

Conclusion: The proposed WASABI method yields a novel simultaneous B_0 and B_1 mapping within 1 min that is robust and easy to implement. **Magn Reson Med 77:571–580, 2017.**

Key words: field mapping; B_0 mapping; B_1 mapping; WASABI; CEST

INTRODUCTION

The homogeneity of the static magnetic (B_0) and radiofrequency (RF) transmit (B_1) field are important quality parameters of MR scanners and coil systems. However, with the tendency to ultrahigh field strength ($\geq$7 T) B_0 and B_1 inhomogeneities also increase. As these inhomogeneities affect the MRI contrast – especially in diffusion-weighted imaging (DWI) and chemical exchange saturation transfer (CEST) imaging – several methods have been developed to compensate for these inhomogeneities.

Basically, these can be divided into two approaches: (1) preacquisition and acquisition methods that directly improve the field homogeneities before or during the measurement such as B_0 shim and parallel transmit technologies (also known as "B_1 shim"), and (2) postprocess correction methods that map and compensate for the inhomogeneities in the acquired data; examples are B_0 and/or B_1 correction of CEST (1–8) and DWI (9–11) contrasts, correction of B_0-inhomogeneity effects in MR thermometry (12) and MR spectroscopic imaging (13), or B_0 and B_1 correction of T_2 maps, employed, eg, in three-dimensional (3D) polymer-gel dosimetry (14). In any case, information about the actual spatial distribution of the B_0 and/or B_1 fields is needed. Usually, those B_0 and B_1 maps are acquired separately using two different MR sequences. Most approaches for B_0 mapping employ phase maps, while common B_1 mapping methods can generally be classified in either magnitude or phase-based methods. Most of the published methods belong to the first class, including all methods that rely on the double-angle method (15), which uses the ratio of two or more magnitude images to estimate local flip angles (16,17). Moreover, a comparison of spin-echo and stimulated-echo magnitude images can be employed to calculate field maps (18). The phase-based methods include, for example, the Bloch-Siegert shift method (BSS) (19) or methods that use phase information created by frequency-modulated pulses (20).

Here we propose a novel method based on Rabi oscillations resulting from off-resonant irradiation that allows the mapping of the water frequency shift ($\delta\omega$) and B_1 amplitude (WASABI) simultaneously. The employed MR sequence is a simple magnetization-prepared sequence similar to a magnetization transfer (MT) or CEST sequence. It consists of a short preparation block (one rectangular pulse with pulse duration $t_p = 5$ ms and nominal RF amplitude $B_1 = 3.7\,\mu$T), followed by a spoiler gradient and a conventional MRI readout. Sampling of several frequency offsets around the water resonance reveals the sinc-shaped saturation spectrum of the pulse, from which the absolute water frequency ω_0 and the B_1 amplitude can be derived.

First, we show how this presaturation scheme can be described mathematically, and how experimental data can be fitted. Second, we investigate the stability of the WASABI approach with regard to the influences of T_1, T_2,

[1]German Cancer Research Center (DKFZ), Medical Physics in Radiology, Im Neuenheimer Feld 280, D–69120 Heidelberg, Germany.

[2]Biomedizinische NMR Forschungs GmbH am Max-Planck-Institut für biophysikalische Chemie, Am Fassberg 11, D-37077 Göttingen, Germany.

*Correspondence to: Patrick Schuenke, MSc, German Cancer Research Center (DKFZ), Division of Medical Physics in Radiology, Im Neuenheimer Feld 280, D–69120 Heidelberg, Germany. Telephone: + 49 6221-42 2533; Fax: + 49 6221-42 2585; E-mail: p.schuenke@dkfz.de

Received 25 September 2015; revised 18 December 2015; accepted 27 December 2015

DOI 10.1002/mrm.26133

Published online 9 February 2016 in Wiley Online Library (wileyonlinelibrary.com).

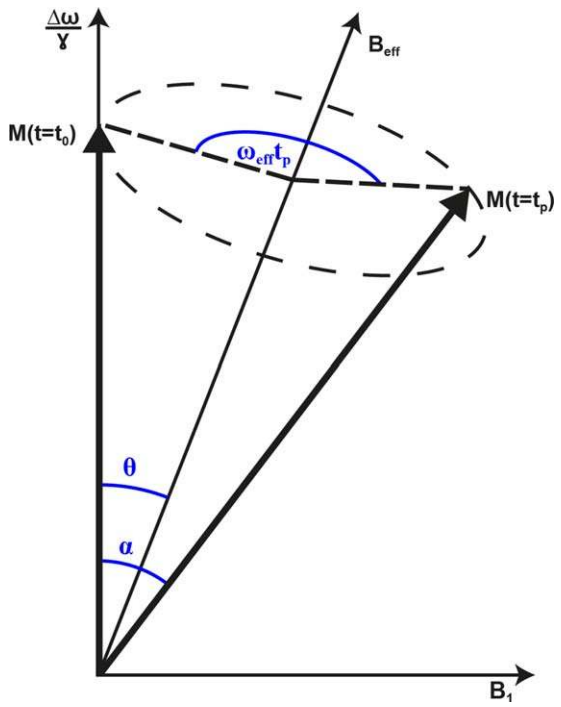

FIG. 1. Precession of the magnetization around the effective field B_{eff}. The rotation angle $\phi = \omega_{eff} \cdot t_p$ depends on the pulse duration t_p, the amplitude B_1 of the excitation field, and the frequency offset $\Delta\omega$.

MT, and repetition time. Finally, we present a simple implementation of WASABI using a gradient echo (GRE) based CEST-MRI sequence that is well-suited for whole-body scanners. It turns out that both B_0 and B_1 maps obtained by WASABI can compete well with maps obtained by standard methods. As a potential application, the correction of field-inhomogeneity effects in CEST-MRI contrast in the human brain at $B_0 = 7\,T$ is demonstrated. Issues concerning scanning time are also discussed.

METHODS

Mathematical Description and Fit Model

Following the approach of Haacke et al, the Bloch equations in the case of short off-resonant irradiation can be solved by neglecting T_1 and T_2 relaxation. Defining $\alpha(t)$ as the angle between the z-axis and $\vec{M}(t)$ (Fig. 1) yields the following expression for the z-magnetization after a block pulse of duration t_p (21)

$$M_z(t_p) = \cos\left(\alpha(t_p)\right) = M_0 \cdot \left\| 1 - 2 \cdot sin^2(\theta) \cdot sin^2\left(\frac{\omega_{eff} \cdot t_p}{2}\right) \right\| \quad [1]$$

With $\tan\theta = \frac{\gamma B_1}{\Delta\omega}$, $\omega_{eff} = \sqrt{(\gamma \cdot B_1)^2 + (\Delta\omega)^2}$, and $Z(\Delta\omega) \equiv \frac{M_z(\Delta\omega)}{M_0}$ we obtain

$$Z(\Delta\omega) = \left\| 1 - 2 \cdot sin^2\left(tan^{-1}\left(\frac{\gamma \cdot B_1}{\Delta\omega}\right)\right) \cdot \sin^2\left(\sqrt{(\gamma \cdot B_1)^2 + (\Delta\omega)^2} \cdot \frac{t_p}{2}\right) \right\| \quad [2]$$

The quantity $\Delta\omega = \omega_{rf} - \omega_0$ is the radiofrequency offset relative to the Larmor frequency ω_0 (for ^1H: $\frac{\omega_0}{B_0} = \gamma = 2\pi \cdot 42.578 \frac{MHz}{T}$). To consider the initial magnetization and relaxation influences during the pulse, we introduce the fit parameters c and d in Eq. [3]. B_0 inhomogeneities cause an additional shift $\delta\omega$ of the frequency in each voxel. Therefore, the actual frequency offset in a voxel is given by $\Delta\omega - \delta\omega$, leading to

$$Z(\Delta\omega) = \left\| c - d \cdot sin^2\left(tan^{-1}\left(\frac{\gamma \cdot B_1}{\Delta\omega - \delta\omega}\right)\right) \cdot sin^2\left(\sqrt{(\gamma \cdot B_1)^2 + (\Delta\omega - \delta\omega)^2} \cdot \frac{t_p}{2}\right) \right\|. \quad [3]$$

With $\Delta\omega$ and the pulse duration t_p as the input, this is a model with four free parameters: c, d, B_1, and $\delta\omega$. While the parameters c and d describe solely the amplitude modulation independent of the frequency offset, the parameter B_1 changes the periodicity and $\delta\omega$ the symmetry axis of the function (Fig. 2). By sampling $Z(\Delta\omega)$ for several frequency offsets around the Larmor frequency of water protons, both the water frequency shift $\delta\omega$ and the B_1 amplitude of the pulse can be determined simultaneously. Passing the adjusted resonance frequency of the measurement system allows the conversion of the determined water-frequency shift $\delta\omega$ into the absolute water frequency ω_0 and therefore the actual field strength B_0.

Bloch Simulations

For simulations, the Bloch-McConnell equations were solved using the expm function of MATLAB (MATLAB R2015a, Natick, Massachusetts) assuming a two-pool model with a bulk water and a MT pool (22). If not stated otherwise, standard simulation parameters were chosen similar to white matter at 3 T (23): $T_1 = 1084$ ms, $T_2 = 69$ ms, relative MT pool-size fraction $f_B = 13.9\%$, $T_{2B} = 9.1\,\mu s$, $k_{BA} = 23\,Hz$. The standard preparation scheme was realized by a rectangular pulse of duration $t_p = 5$ ms and nominal $B_1 = 3.7\,\mu T$. Frequency offsets $\Delta\omega$ were equally

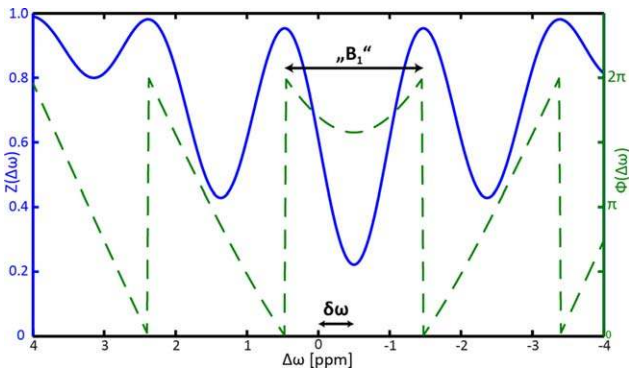

FIG. 2. Simulated Z-spectrum at $B_0 = 3\,T$ generated by saturation by means of a single rectangular pulse with duration $t_p = 5$ ms and amplitude $B_1 = 3.7\,\mu T$ (solid blue line). The maxima occur when the phase (dashed green line) is a multiple of 2π. In this case the magnetization is rotated back in its initial orientation parallel to B_0. Information about the water-frequency shift $\delta\omega$ and the RF amplitude B_1 is encoded in the shift of the symmetry axis and the periodicity of the function $Z(\Delta\omega)$, respectively.

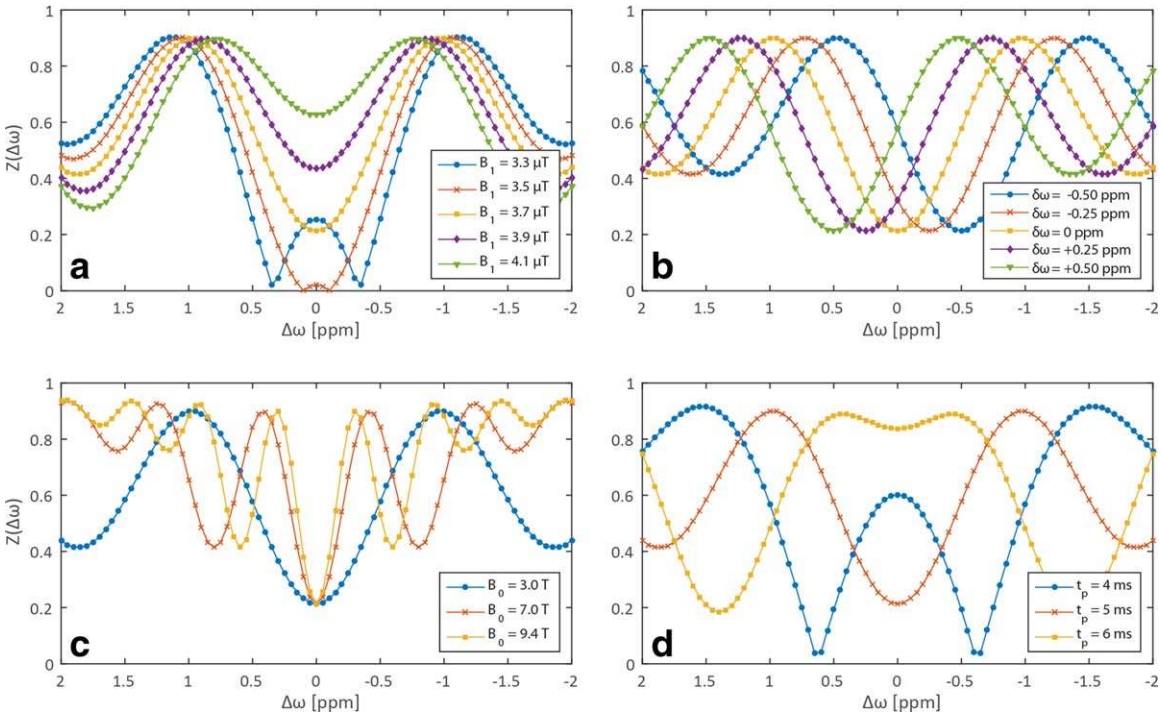

FIG. 3. Simulated WASABI Z-spectra for varying RF amplitudes B_1 (a), water-frequency shifts δω (b), field strengths B_0 (c), and pulse duration t_p (d). The sinc-like response and its dependence on the varied parameters is clearly visible. Sequence and system parameters were $t_p = 5$ ms, $B_1 = 3.7\,\mu$T, $B_0 = 3$ T, $t_{rec} = 3$ s, $T_1 = 1084$ ms, $T_2 = 69$, $f_B = 13.9\%$, $T_{2B} = 9.1\,\mu$s, and $k_{BA} = 23$ Hz.

spaced between −2 and +2 ppm in steps of 0.05 ppm, and a recovery time (t_{rec}) = 3 s was included between the different offsets, allowing the magnetization to recover. The initial magnetization before the recovery time was $0.1 \cdot M_0$. Using these settings, the Z-spectra for different RF amplitudes B_1 (Fig. 3a), water-frequency shifts δω (Fig. 3b), field strengths B_0 (Fig. 3c), pulse durations t_p (Fig. 3d), longitudinal and transversal relaxation times T_1 and T_2 (Fig. 4a and 4b), recovery times t_{rec} (Fig. 4c), and different MT pool-size fractions f_B (Fig. 4d) have been simulated.

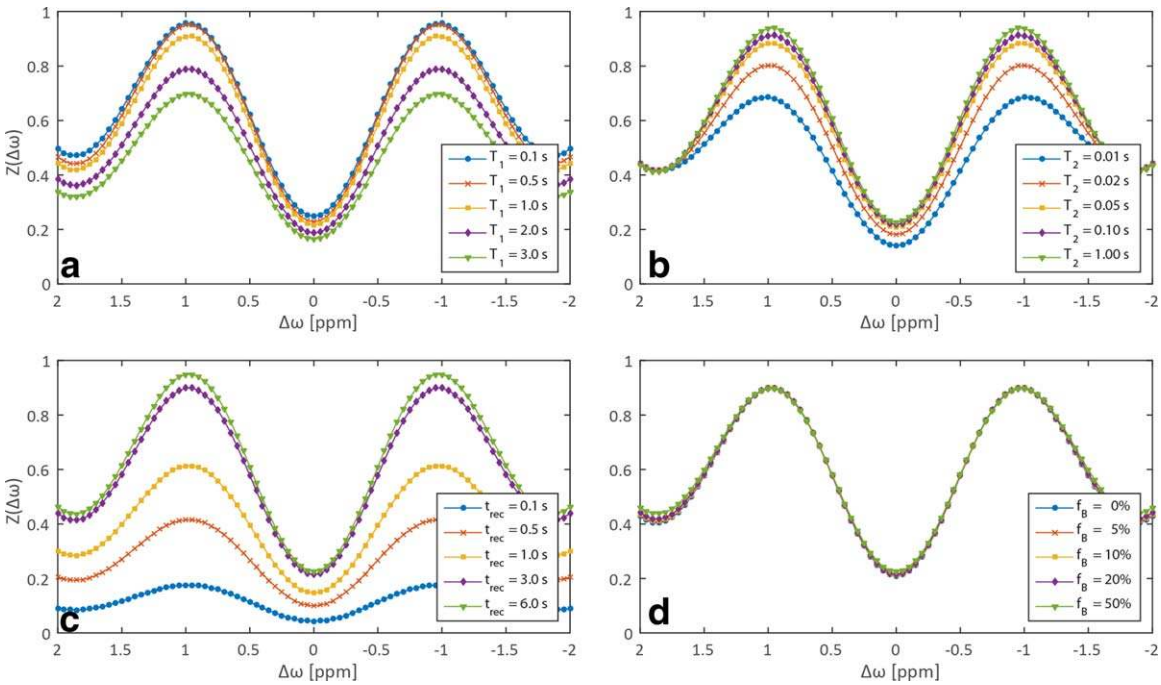

FIG. 4. Simulated WASABI Z-spectra at $B_0 = 3$ T for different longitudinal relaxation times T_1 (a), transversal relaxation times T_2 (b), recovery times (t_{rec}) between the different offsets (c), and MT pool-size fractions f_B (d). Standard values (if not varied) were $t_{rec} = 3$ s, $T_1 = 1084$ ms, $T_2 = 69$ ms, $f_B = 13.9\%$, $T_{2B} = 9.1\,\mu$s, and $k_{BA} = 23$ Hz; for the rectangular preparation pulse, $t_p = 5$ ms and $B_1 = 3.7\,\mu$T.

Volunteers

MR measurements were performed on three healthy male volunteers (age 24 ± 5 years). The examinations were approved by the local ethics committee of the Medical Faculty at the University of Heidelberg.

MR Measurements

All measurements were performed on whole-body MRI scanners with static field strengths $B_0 = 3$ T (Biograph mMR, Siemens Healthcare, Erlangen, Germany) and $B_0 = 7$ T (MAGNETOM, Siemens Healthcare, Erlangen, Germany), respectively, using a 16-channel head/neck coil at the 3T scanner and a transmit and receive (Tx: 1 channel, Rx: 24 channel) head coil at the 7T scanner.

B_0 and B_1 Mapping

The MR sequence used for WASABI measurements is similar to a CEST sequence and consists of a short preparation block followed by a conventional MRI readout. For the MRI readout, a two-dimensional (2D) single-shot gradient echo sequence (GRE) as described in Ref. 24 was used. The imaging parameters were echo time (T_E) = 3.61 ms, repetition time (T_R) = 7.4 ms, field of view (FOV) = $200 \times 200\,mm^2$, matrix = 128×128, flip angle = 10°, slice thickness = 5 mm at $B_0 = 7$ T and $T_E = 3.63$ ms, $T_R = 7.7$ ms, FOV = $177 \times 210\,mm^2$, matrix = 128×128, flip angle = 10°, and slice thickness = 5 mm at $B_0 = 3$ T. For preparation, a rectangular pulse with a pulse duration $t_p = 5$ ms and nominal $B_1 = 3.7\,\mu T$ (on-resonant flip angle = 284°) was applied. Sampling of various offsets ($n = 7$–81) was performed equidistantly between $\Delta\omega = \pm 1.5$ ppm and $\Delta\omega = \pm 2$ ppm at 7 T and 3 T, respectively. An additional M_0 image at $\Delta\omega$ = -300 ppm was acquired for normalization. For comparison of B_1 inhomogeneity maps, the Bloch-Siegert Shift (BSS) method was employed, using the same FOV and matrix size as for the WASABI measurements. The BSS method was chosen as reference, because it is a fast and robust method, which is in good agreement with the widely used double-angle method (19). The parameters of the used off-resonant Fermi-shaped pulse were peak amplitude $B_{1,max} = 10\,\mu T$, off-resonance frequency $\omega_{RF} = 6$ kHz. The Ernst angle was chosen as the imaging flip angle, and T_E and T_R were chosen as short as possible: $T_E = 12$ ms, $T_R = 585$ ms at $B_0 = 7$ T and $T_R = 300$ ms at $B_0 = 3$ T. For comparison of B_0 inhomogeneity maps, an appropriately tuned version of the water saturation shift referencing (WASSR) method (1) (1 Gaussian-shaped pulse, $t_p = 25$ ms, nominal $B_1 = 0.2\,\mu T$) was employed using the same imaging readout and the same frequency offsets as for the WASABI measurements. Measurement times were approximately 2:35 min for each WASABI and WASSR, and approximately 2:30 min for the BSS method.

CEST Measurements

For CEST measurements, the same GRE sequence as for the WASABI was employed. The imaging parameters were $T_E = 3.1$ ms, $T_R = 6.4$ ms, FOV = $183 \times 210\,mm^2$, matrix = 128×128, flip angle = 10°, slice thickness = 5 mm. For saturation, a pulse train of 150 Gaussian-shaped pulses with pulse duration $t_p = 15$ ms, duty cycle = 60%, recovery time $t_{rec} = 3$ s, and RF amplitudes $B_1 = 0.5$, 0.65, 0.8, 0.95, and 1.1 μT were applied. Sampling of $n = 59$ frequency offsets was performed unevenly between $\Delta\omega = \pm 8$ ppm; normalization was done as for the WASABI measurements using an additionally acquired M_0 image at $\Delta\omega = -300$ ppm. The measurement time for each CEST experiment was 7:09 min.

Data Analysis

All data analyses were performed using self-written software in MATLAB. Analysis of measured WASABI data can be separated into the following steps: First, voxels in the M_0 image with intensities smaller than 10% of the maximum intensity were assumed to be background and excluded from the analysis. Second, the intensities of all remaining voxels were normalized using the M_0 image acquired at $\Delta\omega = -300$ ppm. In the third step, a lookup table with Z-spectra for all possible combinations of the four fit parameters *c, d*, B_1, and δω was created to increase the robustness and efficiency of the fitting process. The lookup-table parameter space was chosen as follows: $c = [0.2{:}0.05{:}1]$, $d = [0.5{:}0.1{:}2.0]$, $B_1 = [1.0{:}0.15{:}5.55]$, and $\delta\omega = [-1{:}0.025{:}1]$. In the next step, the parameter set with the lowest absolute difference between the simulated Z-spectrum and the measured data was determined for each voxel. Finally, Eq. [3] was fitted to the acquired data of each voxel using the parameter sets determined in the previous step as the starting parameters for the fit. The fit yielded simultaneously the maps of the four fit parameters including the water-frequency shift (δω) and the B_1 amplitude. As an optimization algorithm, a Levenberg-Marquardt algorithm (25) was employed. Data analysis of WASSR and BSS data was performed as described in the original publications of Kim et al (1) and Sacolick et al (19), respectively. The phase-unwrapping algorithm used for the analysis of the BSS data is based on Maier et al (26). In the end, the mask generated in the first step of the WASABI data analysis was applied to the maps obtained by application of WASSR and BSS.

RESULTS

Bloch-McConnell Simulations

As predicted by the analytical expression (Eq. [2]), the simulated Z-spectra (using the full Bloch-McConnell equation system) vary upon changes of the RF amplitude B_1 (Fig. 3a) and the water-frequency shift δω (Fig. 3b). A decrease in the static magnetic field strength B_0 causes a broadening of the spectral response (Fig. 3c), which can in principle be adapted by adjusting the pulse duration t_p (Fig. 3d). The offset range to be sampled is defined by the expected shift of the water frequency. For in vivo measurements in the brain at high and ultrahigh-field whole-body scanners, we assumed a maximum shift of approximately ±1 ppm, and hence sampled the offsets between ± 1.5 ppm at $B_0 = 7$ T and ± 2.0 ppm at 3 T, keeping a constant pulse duration ($t_p = 5$ ms) and constant RF amplitude ($B_1 = 3.7\,\mu T$). This yields an appropriate sampling of the induced Rabi oscillations at both field strengths.

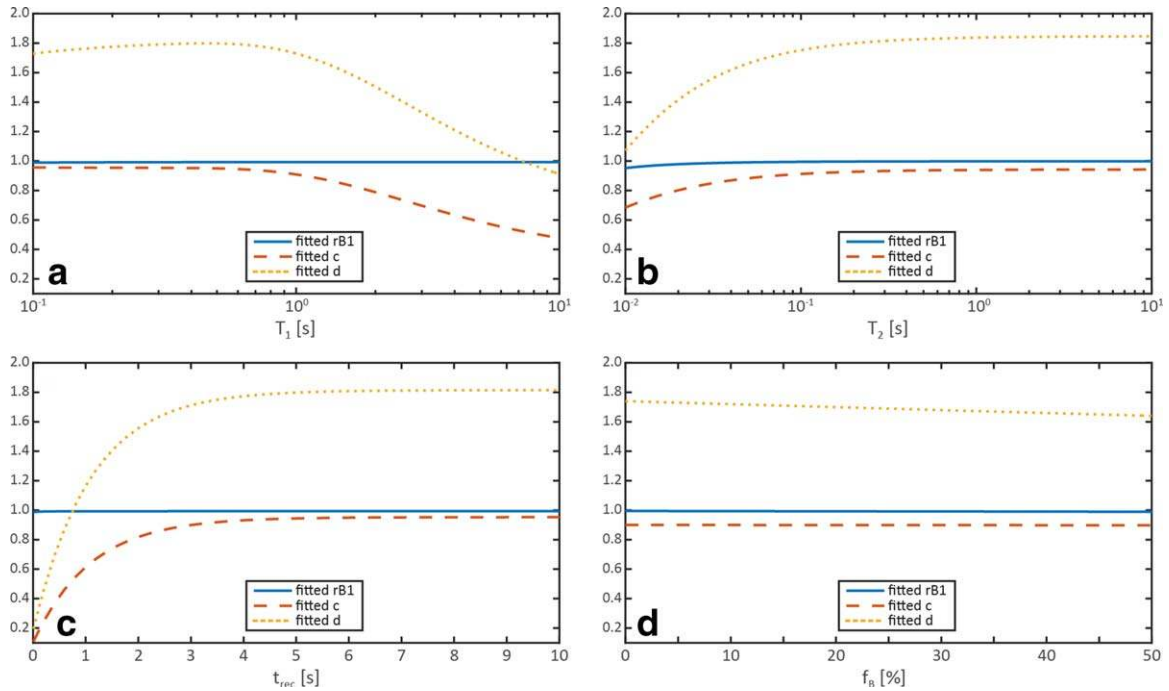

FIG. 5. WASABI-fit results for simulated spectra. WASABI parameters rB_1 (solid blue line), *c* (dashed red line), and *d* (dotted yellow line) as a function of longitudinal relaxation time T_1 (a), transversal relaxation time T_2 (b), recovery time t_{rec} (c), and MT pool-size fraction f_B (d). Fit results for $\delta\omega$ are not shown, as deviations were smaller than 10^{-9} in each case. For the standard sequence and system settings, see Figures 3 and 4.

To verify the robustness of the WASABI method against changes in relaxation parameters, we performed additional simulations. Figure 4 shows the simulated Z-spectra for various T_1 and T_2 relaxation times (Fig. 4a and 4b), recovery times t_{rec} (Fig. 4c), and MT pool-size fractions f_B (Fig. 4d). Especially for changes of T_1, T_2, and t_{rec}, the shape of the Z-spectra varies significantly with respect to baseline and amplitude of the induced Rabi oscillations. However, the symmetry axis and the periodicity of the Z-spectra appear to remain unaffected. Therefore, these variations should be compensated by the fit parameters *c* and *d* and have no influence on the obtained values of $\delta\omega$ and B_1. To prove this, we performed further simulations by varying T_1, T_2, t_{rec}, and f_B over large ranges and fitted the generated Z-spectra using Eq. [3]. Figure 5 shows the fit results for *c, d*, and the relative B_1 amplitude (rB_1) plotted as a function of T_1, T_2, t_{rec}, and f_B. As the fit results for $\delta\omega$ were smaller than 10^{-9} in all cases, the fitted $\delta\omega$ are not shown. For the complete range of simulated T_1 and t_{rec} (both 0.1–10 s), the variations in the simulated Z-spectra were compensated by the fit parameters *c* and *d*. Changes in both parameters become prominent for $t_{rec} < 3 \cdot T_1$, which reflects the actual recovery state; this indicates that the added parameters correctly compensate for relaxation effects. However, observed deviations of fitted rB_1 are smaller than 1% for the complete parameter range (Fig. 5a and 5c). This also applies to simulated T_2 (0.045–10 s) and f_B (0–45%). For T_2 between 45 and 20 ms, deviations remain smaller than 2% and smaller than 5% for simulated values shorter than 20 ms. As all simulations were performed under conditions of optimum signal-to-noise ratio (SNR), we also investigated the influence of the SNR on the fitted parameters. The outcome of these simulations is included in the Supporting Material (Sup. Fig. S1). The simulations show that a SNR > 20 is required for reliable determination of rB_1 and $\delta\omega$.

Application of WASABI in Vivo

The introduction of the fit parameters *c* and *d* thus allowed quantitative access to the water-frequency shift $\delta\omega$ and RF amplitude B_1 in vivo. Figure 6a and 6b shows the acquired data (red dots) of two representative voxels in the brain of a healthy volunteer at $B_0 = 3$ T. Although the shape of both Z-spectra is completely different, the WASABI fit (solid blue lines) matches the measured data very well. Pixel-wise evaluation yields the four simultaneously generated parameter maps displayed in Figure 6c–6f. Both the $\delta\omega$ and rB_1 map appear smooth and show no anatomical structure. As expected, all relaxation influences appear to be modeled by the fit parameters *c* and *d*, leading to some anatomical contrast resolved in the maps of *c* (Fig. 6e) and *d* (Fig. 6f).

Comparison with WASSR and BSS at 3 T and 7 T

The $\delta\omega$ and rB_1 maps obtained by the WASABI method could now directly be compared with the outcome of alternative mapping techniques, namely, the WASSR method for $\delta\omega$ mapping and the BSS method for B_1 mapping. All maps obtained by WASABI, WASSR, and BSS are presented in Figure 7a–7d. The aspect of both $\delta\omega$ and both rB_1 maps is similar. The maps obtained by WASABI look even a bit smoother, although the SNR of the individual images of BSS (SNR = 194, number of excitations (NEX) = 2) and WASSR (SNR = 84, NEX = 32) was greater

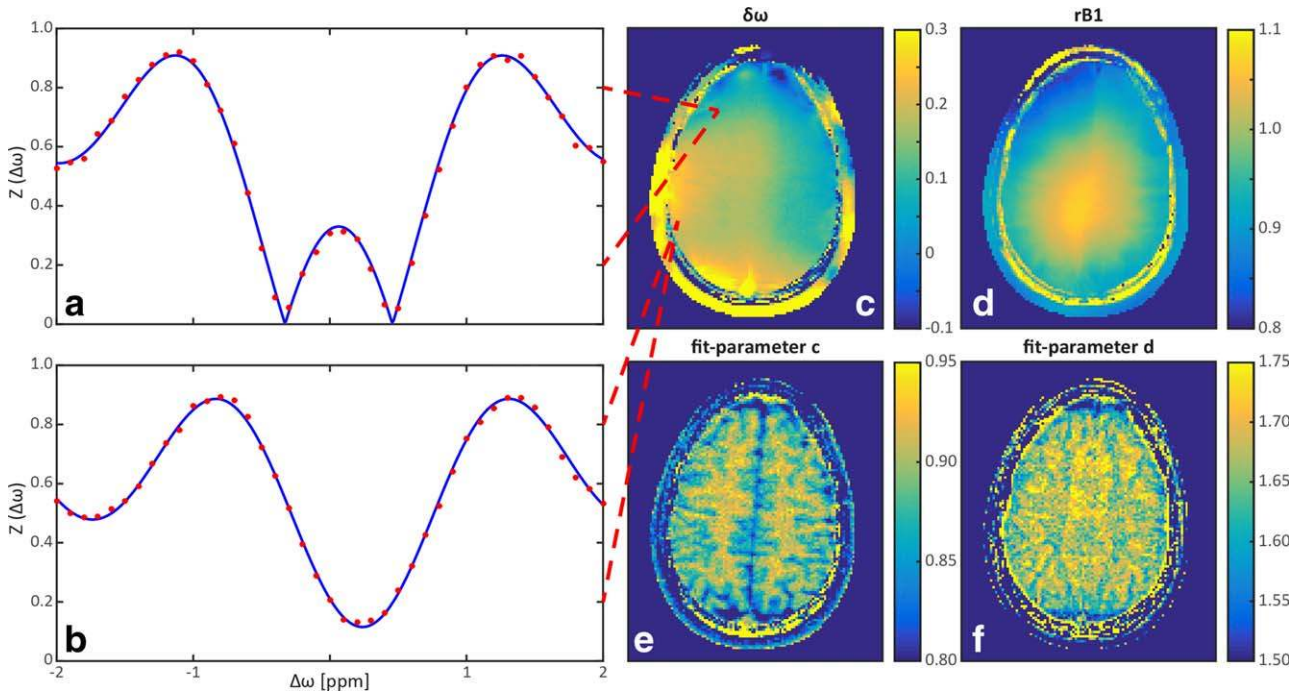

FIG. 6. Application of WASABI to image data from the brain of a healthy volunteer obtained at $B_0 = 3$ T: two measured single-voxel Z-spectra (red dots) together with the WASABI fit (solid blue line) (a, b); and resulting parameter maps for δω (c), rB_1 (d), *c* (e), and *d* (f).

or equal to WASABI (SNR = 84, NEX = 32). To evaluate the correlation between WASABI and the reference techniques quantitatively, Bland-Altman plots of the obtained δω and rB_1 values in a large region of interest (ROI) in the brain (4803 voxels) are shown in Figure 7e and 7f. The differences ($\delta\omega_{diff}$ and $rB1_{diff}$) are calculated by subtracting the reference values from the values obtained by the WASABI method. The plots show that the WASABI method is in good agreement with both reference techniques (mean $\delta\omega_{diff} = -0.0035$ ppm $\triangleq$ 0.4 Hz, mean $rB1_{diff} = 0.88\%$). The same evaluation process was applied to data acquired at $B_0 = 7$ T from the brain of another healthy volunteer. The corresponding δω and rB_1 maps obtained by WASABI, WASSR, and BSS are shown in Figure 8a–8d, while the Bland-Altman plots of the δω and rB_1 values (ROI of 5810 voxels) are displayed in Figure 8e and 8f. Because of larger B_1 inhomogeneities at $B_0 = 7$ T (compared with the 3T case), the values of rB_1 vary over a larger range, but again the values obtained by WASABI are in good agreement with the reference methods (mean $\delta\omega_{diff} = -0.0081$ ppm, mean $rB1_{diff} = -1.87\%$).

Exemplary Application: Correction of Field-Inhomogeneity Effects in CEST Z-Spectra

As a potential application of B_0 and B_1 mapping by means of WASABI, the correction of field-inhomogeneity effects in CEST Z-spectra is proposed. Data were obtained from the brain tissue of a healthy volunteer at $B_0 = 7$ T; two ROIs (marked in the MR image shown in the bottom-left corner in Fig. 9a) were placed in different areas of gray matter. The mean water-frequency shift and relative RF amplitude were $\delta\omega = (-1.4 \pm 1.6)$ Hz, $rB_1 = (0.85 \pm 0.03)$ μT in the first ROI and $\delta\omega = (43.8 \pm 6.7)$ Hz, $rB_1 = (1.10 \pm 0.02)$ μT in the second ROI. Accordingly, the uncorrected ROI-averaged Z-spectra displayed in Figure 9a do not match. After correction for B_0 inhomogeneities by linear interpolation and frequency shift, the symmetry axes of both Z-spectra agree well. However, Figure 9b reveals that off-resonant Z-values still differ as a consequence of unequal labeling expected from the discrepancy of rB_1 in both ROIs (27–29). Therefore, the B_0-corrected Z-spectra were further corrected for B_1 inhomogeneities by means of the 5-point Z-B_1-correction proposed by Windschuh et al (5). Employing the obtained B_1 values ($B_1 = 0.5$ μT, 0.65 μT, 0.80 μT, 0.95 μT, and 1.10 μT), the Z-spectra of all voxels were interpolated to $B_1 = 0.65$ μT, leading to a very good match of the two ROI-averaged Z-spectra (Fig. 9c).

DISCUSSION

In this study we introduce a new method for simultaneous mapping of the water-frequency shift and the RF amplitude based on Rabi oscillations induced by off-resonant irradiation. This so-called WASABI method samples the data Z(Δω) at several frequency offsets around the water proton resonance after off-resonant irradiation with a short rectangular pulse. The quasi sinc-shaped spectral response to this excitation yields values of δω and B_1, which are encoded in the shift of the symmetry axis and the periodicity of the function Z(Δω), respectively (Fig. 2).

B_1 Mapping

Various B_1–mapping methods have been developed so far, most of which employ magnitude information; others use phase information. Our WASABI method is a hybrid method, insofar as it uses the signal magnitude modulated

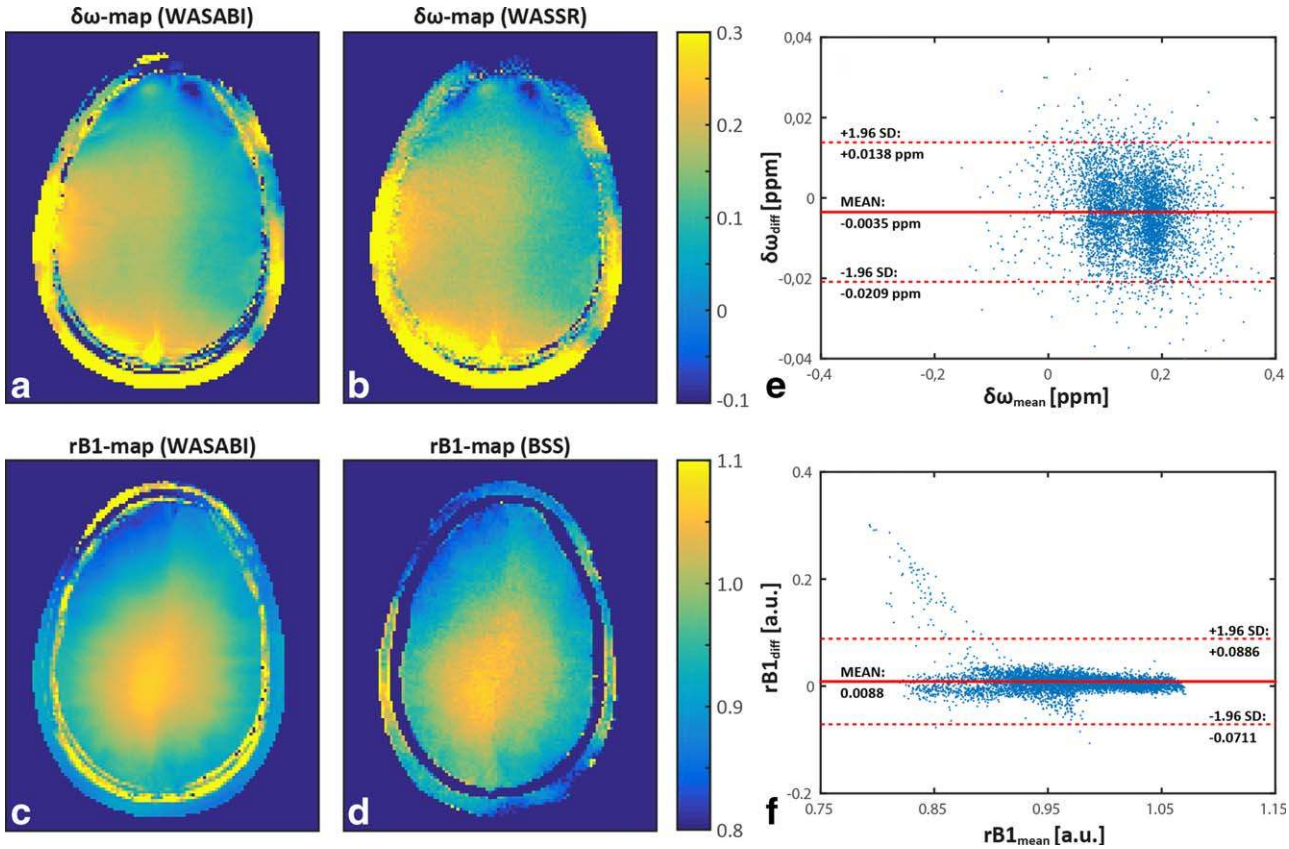

FIG. 7. Comparison of field-inhomogeneity maps obtained at $B_0 = 3\,T$ by means of WASABI and alternative methods: δω map using WASABI (a), δω map using WASSR (b), rB_1 map using WASABI (c), rB_1–map using BSS (d), Bland-Altman plot of the δω values obtained by WASABI and WASSR (e), and Bland-Altman plot of the rB_1 values obtained by WASABI and BSS (f).

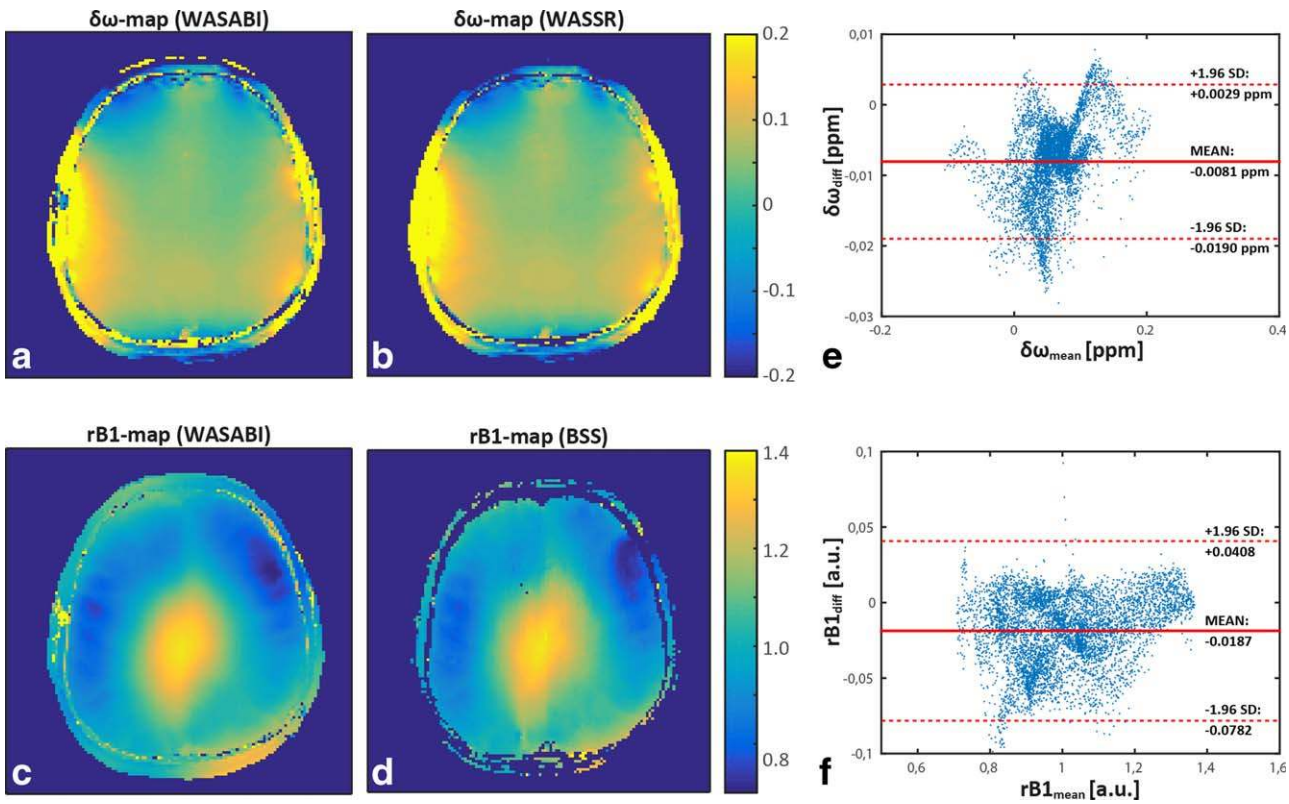

FIG. 8. Comparison of field-inhomogeneity maps obtained at $B_0 = 7\,T$ by means of WASABI and alternative methods: δω map using WASABI (a), δω map using WASSR (b), rB_1 map using WASABI (c), rB_1 map using BSS (d), Bland-Altman plot of the δω values obtained by WASABI and WASSR (e), and Bland-Altman plot of the rB_1 values obtained by WASABI and BSS (f).

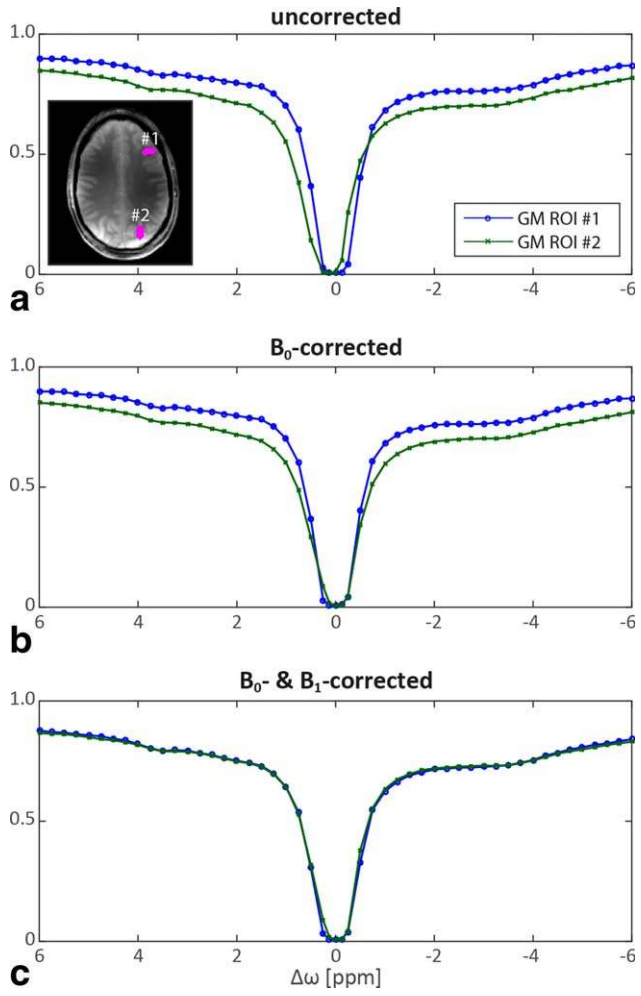

FIG. 9. Correction of field-inhomogeneity effects in CEST Z-spectra acquired from the brain tissue of a healthy volunteer at $B_0 = 7$ T: uncorrected ROI-averaged Z-spectra from two ROIs placed in gray matter regions (marked in the MR image shown in the bottom-left corner) (a), B_0-corrected Z-spectra from ROI-averaged data (b), and B_0- and B_1-corrected Z-spectra of the same data (c). CEST settings: 150 Gaussian-shaped pulses with duration $t_p = 15$ ms, duty cycle = 60%, recovery time $t_{rec} = 3$ s, and $B_1 = 0.5$, 0.65, 0.8, 0.95, and 1.10 μT.

by irradiation of an off-resonant rectangular pulse. A limitation of all approaches that rely on magnitude is that absolute values depend on T_1 (and hence on the repetition time TR) and on relaxation during the RF pulses. Following the rule, "never measure intensities but frequencies," the WASABI method translates the B_1 dimension to the better-defined Larmor frequency dimension. Thus, WASABI overcomes this problem, because the frequency of the sinc-like response does not depend on relaxation. By introducing the two additional-fit parameters *c* and *d* in Eq. [3], a model could be established that compensates for the relaxation effects. This could be verified by fitting relaxation-affected data using the final WASABI equation (Eq. [3]) with less than 1% deviations in $\delta\omega$ and rB_1 (Fig. 5), independent of varied relaxation parameters. Likewise, WASABI applied to in vivo data showed structural contrast only in the maps of *c* and *d* (Fig. 6). The obtained maps for parameters *c* and *d* show larger values mostly in white-matter regions, where T_1 is expected to be smaller compared with gray matter (23). This is in agreement with the simulations shown in Figure 5a, where we observed decreasing values of parameters *c* and *d* for increasing T_1.

B_0 Mapping

Traditional field-mapping approaches are used primarily for B_0 shim; therefore, a relative inhomogeneity map is sufficient instead of an absolute water-frequency map. However, in some applications, knowledge about the exact water-frequency shift in each voxel is needed, as demonstrated for the correction of CEST Z-spectra in this study. Another method that enables water-frequency-shift mapping is the WASSR method (1), which employs off-resonant low-power RF pulses to acquire pure direct-water-saturation images. Analogous to WASABI, sampling of several frequency offsets around the water resonance leads to a Z-spectrum that is symmetric, and, in the case of WASSR, minimal at the actual water proton frequency in the voxel. Even though the effective SNR can be increased by Lorentzian fitting (30,31), determination of a minimum in principle suffers from low SNR. Still, WASSR is used widely in CEST studies, as the image contrast and the WASSR Z-spectrum, according to Kim et al, can be obtained "using identical acquisition schemes, avoiding a mismatch in field-based image distortions between the two data sets" (1). This statement also holds for WASABI, where, contrary to WASSR, the information about the symmetry axis is additionally stored in the maxima of the induced Rabi oscillations. The SNR of the maxima can be adjusted more effectively, eg, by T_R (Fig. 4c). Similar to WASSR, WASABI can also be used for quantitative susceptibility mapping (31).

Simple and Simultaneous B_1 and B_0 Mapping

In terms of scanning time, flip-angle methods for B_1 mapping and phase methods for B_0 mapping are by far faster than WASABI with approximately two readout scans for both conventional B_0 and B_1 mapping, but approximately 20 readouts for WASABI. For example, the dual refocusing echo acquisition mode (DREAM) (32) method allows B_1 mapping of the entire human brain in less than 20 s, and is therefore up to one order of magnitude faster than WASABI, even if the latter is optimized. Therefore, WASABI may not be the method of choice if measurement time is crucial, but WASABI has several benefits: The first benefit is the simultaneous generation of B_0 and B_1 maps. Because the position of the symmetry axis and the frequency are independent features, possible B_1 inhomogeneities do not affect the determination of B_0 and vice versa. This is rather a problem of other field-mapping methods. The second benefit is that the implementation of WASABI is simple – and using magnitude images – does not depend, in principle, on the readout mode of image data. This allows the use of only slightly modified sequences for B_0 and B_1 mapping compared with the sequences required for acquisition of magnetization-prepared MRI contrasts. The third benefit is that the employed preparation pulse has the same

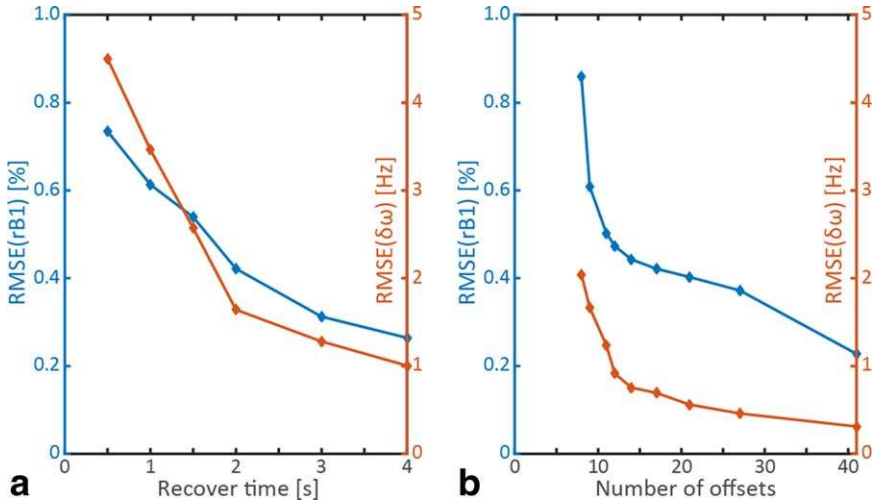

FIG. 10. Deviations (root mean square error) of fitted rB_1 and $\delta\omega$ for constant number of offsets ($n = 31$) and different recovery times (t_{rec}) (a), and constant $t_{rec} = 2$ s and different number of offsets (b). The reference values were obtained with $t_{rec} = 5$ s and $n = 81$, respectively. The gain in accuracy is small for recovery times larger than 2 s and sampling with more than 20 offsets.

power and duration for all irradiated offsets, which is beneficial because (1) relaxation during the preparation pulse is always the same; and (2) by using a single power level, any nonlinearity in the RF amplifier does not affect the determination of B_1. Last but not least, storing information in the z-magnetization has the benefit that a delay between the magnetization preparation and the image readout can be inserted to avoid potential field distortions resulting from eddy currents.

Limitations and Convergence Intervals

The WASABI method is prone to influences of the starting values of the fit because of the nonlinearity of the signal model (Eq. [3]). To avoid local minima during the fitting process, a lookup table with WASABI Z-spectra for all possible combinations of the four fit parameters $\delta\omega$, rB_1, c, and d was created before applying the actual fitting algorithm. The best match of this preoptimization leads to good start values for each voxel and is necessary to provide a robust outcome of the fitting process.

To accelerate the WASABI sequence, both the recovery time and the number of sampled offsets can be reduced (Fig. 10). As expected, the mean deviation increases with decreasing t_{rec} (Fig. 10a) or less offsets (Fig. 10b), but deviations of B_1 and $\delta\omega$ remain below 0.5% and 2 Hz, respectively, for $t_{rec} \geq 2$ s and $n \geq 21$. Hence, we suggest the following settings for fast and reliable field-inhomogeneity mapping in the human brain by means of WASABI: pulse duration $t_p = 5$ ms, RF amplitude $B_1 = 3.7\,\mu T$, offset range $\Delta\omega = -2$ to 2 ppm at 3 T and $\Delta\omega = -1.5$ to 1.5 ppm at 7 T, number of offsets $n \geq 21$, recovery time between the different offsets $t_{rec} \geq 2$ s (in general we suggest $t_{rec} \geq T_1$; see also Figs. 4 and 5). These values lead to a total acquisition time of approximately 1 min using a GRE readout. Because WASABI is fully compatible with any imaging readout (eg, echo planar imaging (EPI)) or imaging acceleration method, a further decrease of the acquisition time or an increased number of measured slices is possible. These are rules that apply to studies of the human brain; in other organs the offset range and the number of offsets might need to be adjusted because of larger inhomogeneities or different SNR.

Altogether, the proposed WASABI method is in good agreement with alternative B_0 and B_1 mapping techniques (Figs. 7 and 8). For a better understanding of the remaining deviations and a judgment about accuracy and dynamic range, a comprehensive study is required, including a comparison of different optimized mapping techniques. In particular, the widely used double-flip angle methods for B_1 mapping (15–17) should be compared with WASABI with field probes as a reference. We believe that for fast B_1 and B_0 field estimates, double-flip angle methods and conventional phase maps are useful, but because of the benefits described previously, the WASABI method forms a valuable alternative especially for precise and independent mapping of B_1 and B_0.

Application for CEST Correction

The application of WASABI maps to inhomogeneity-artifact correction of CEST data showed clear improvement of the data. Based on a CEST or MT sequence, the WASABI method is easy to realize and is compatible with former correction algorithms for B_0 (1–3) and B_1 (3–5) applied to CEST data. However, the correction of CEST data is only one of the possible applications of WASABI.

CONCLUSIONS

We describe a new method for B_0 and B_1 mapping based on off-resonant irradiation by means of a short rectangular pulse. With an approximate measurement time of 1 min in single-slice mode, the WASABI method is not the fastest field-mapping approach; however, it yields B_0 and B_1 maps simultaneously and is easy to implement for different imaging readouts. A comparison with the outcome of WASSR B_0 mapping and Bloch-Siegert B_1 mapping in studies with human volunteers at 3 T and 7 T showed that the method is well-suited for in vivo applications. The methods permit not only the tracking of field inhomogeneities, but also the correction of MR

image contrasts as demonstrated for the case of B_0 and B_1 correction of CEST-MRI data.

ACKNOWLEDGMENTS

We thank Aaron Kujawa, MSc, for providing the BSS sequence and evaluation script.

REFERENCES

1. Kim M, Gillen J, Landman BA, Zhou J, van Zijl PCM. Water saturation shift referencing (WASSR) for chemical exchange saturation transfer (CEST) experiments. Magn Reson Med 2009;61(6):1441–1450.
2. Zhou J, Payen J-F, Wilson DA, Traystman RJ, van Zijl PCM. Using the amide proton signals of intracellular proteins and peptides to detect pH effects in MRI. Nature Med 2003;9(8):1085–1090.
3. Sun PZ, Farrar CT, Sorensen AG. Correction for artifacts induced by B_0 and B_1 field inhomogeneities in pH-sensitive chemical exchange saturation transfer (CEST) imaging. Magn Reson Med 2007;58(6): 1207–1215.
4. Singh A, Cai K, Haris M, Hariharan H, Reddy R. On B_1 inhomogeneity correction of in vivo human brain glutamate chemical exchange saturation transfer contrast at 7T. Magn Reson Med 2013;69(3):818–824.
5. Windschuh J, Zaiss M, Meissner J-E, Paech D, Radbruch A, Ladd ME, Bachert P. Correction of B_1-inhomogeneities for relaxation-compensated CEST imaging at 7 T. NMR Biomed 2015;28(5):529–537.
6. Meissner J-E, Goerke S, Rerich E, Klika KD, Radbruch A, Ladd ME, Bachert P, Zaiss M. Quantitative pulsed CEST-MRI using Ω-plots. NMR in Biomed 2015;28(10):1196–1208.
7. Zaiss M, Windschuh J, Paech D, Meissner J-E, Burth S, Schmitt B, … Radbruch A. Relaxation-compensated CEST-MRI of the human brain at 7T: Unbiased insight into NOE and amide signal changes in human glioblastoma. NeuroImage 2015;112;180–188.
8. Zaiss M, Windschuh J, Goerke S, Paech D, Meissner JE, Burth S, Kickingereder P, Wick W, Bendszus M, Schlemmer HP, Ladd M, Bachert P, Radbruch A. Downfield NOE-suppressed amide-CEST-MRI at 7 Tesla provides a unique contrast in human glioblastoma. Magn Reson Med 2017;77;196–208.
9. Jezzard P, Balaban RS. Correction for geometric distortion in echo planar images from B_0 field variations. Magn Reson Med 1995;34(1):65–73.
10. Reber PJ, Wong EC, Buxton RB, Frank LR. Correction of off resonance-related distortion in echo-planar imaging using EPI-based field maps. Magn Reson Med 1998;39(2):328–330.
11. Jones DK, Cercignani M. Twenty-five pitfalls in the analysis of diffusion MRI data. NMR Biomed 2010;23(7):803–820.
12. Mei C-S, Chu R, Hoge WS, Panych LP, Madore B. Accurate field mapping in the presence of B_0 inhomogeneities, applied to MR thermometry. Magn Reson Med 2015;73(6):2142–2151.
13. Arteaga de Castro CS, Boer VO, Luttje MP, van der Velden TA, Bhogal A, van Vulpen M, Luijten PR, van der Heide UA, Klomp DWJ. Temporal B_0 field variation effects on MRSI of the human prostate at 7 T and feasibility of correction using an internal field probe. NMR Biomed 2014;27(11):1353–1360.
14. Vandecasteele J, De Deene Y. On the validity of 3D polymer gel dosimetry. II: physico-chemical effects. Phys Med Biol 2013;58(1):43–61.
15. Insko EK, Bolinger L. Mapping of the radiofrequency field. J Magn Reson A 1993;103(1):82–85.
16. Stollberger R, Wach P. Imaging of the active B_1 field in vivo. Magn Reson Med 1997;38(2):336–336.
17. Cunningham CH, Pauly JM, Nayak KS. Saturated double-angle method for rapid B1 + mapping. Magn Reson Med 2006;55(6):1326–1333.
18. Jiru F, Klose U. Fast 3D radiofrequency field mapping using echo-planar imaging. Magn Reson Med 2006;56(6):1375–1379.
19. Sacolick LI, Wiesinger F, Hancu I, Vogel MW. B1 mapping by Bloch-Siegert shift. Magn Reson Med 2010;63(5):1315–1322.
20. Park J-Y, Garwood M. B_1 mapping using phase information created by frequency-modulated pulses. In Proceedings of the 16th Annual Meeting of ISMRM, Toronto, Canada, 2008. p. 361.
21. Haacke E, Brown RW, Thompson MR, Venkatesan R. Magnetic resonance imaging: physical principles and sequence design, New York: A John Wiley and Sons; 1999.
22. Zaiss M, Bachert P. Exchange-dependent relaxation in the rotating frame for slow and intermediate exchange—modeling off-resonant spin-lock and chemical exchange saturation transfer. NMR Biomed 2013;26(5):507–518.
23. Stanisz GJ, Odrobina EE, Pun J, Escaravage M, Graham SJ, Bronskill MJ, Henkelman RM. T1, T2 relaxation and magnetization transfer in tissue at 3T. Magn Reson Med 2005;54(3):507–512.
24. Schmitt B, Zaiß M, Zhou J, Bachert P. Optimization of pulse train presaturation for CEST imaging in clinical scanners. Magn Reson Med 2011;65(6):1620–1629.
25. Lourakis MIA. levmar: Levenberg-Marquardt nonlinear least squares algorithms in {C}/{C}++. 2004 [accessed 2015 Sep 25] http://www.ics.forth.gr/~lourakis/levmar/
26. Maier F, Fuentes D, Weinberg JS, Hazle JD, Stafford RJ. Robust phase unwrapping for MR temperature imaging using a magnitude-sorted list, multi-clustering algorithm. Magn Reson Med 2015;73(4):1662–1668.
27. Liu D, Zhou J, Xue R, Zuo Z, An J, Wang DJJ. Quantitative characterization of nuclear overhauser enhancement and amide proton transfer effects in the human brain at 7 Tesla. Magn Reson Med 2013;70(4): 1070–1081.
28. Roeloffs V, Meyer C, Bachert P, Zaiss M. Towards quantification of pulsed spinlock and CEST at clinical MR scanners: an analytical interleaved saturation-relaxation (ISAR) approach. NMR Biomed 2015;28(1):40–53.
29. Zaiss M, Bachert P. Chemical exchange saturation transfer (CEST) and MR Z-spectroscopy in vivo: a review of theoretical approaches and methods. Phys Med Biol 2013;58(22):R221–R269.
30. Liu G, Qin Q, Chan KWY, Li Y, Bulte JWM, McMahon MT, van Zijl PCM, Gilad AA. Non-invasive temperature mapping using temperature-responsive water saturation shift referencing (T-WASSR) MRI. NMR Biomed 2014;27(3):320–331.
31. Lim IAL, Li X, Jones CK, Farrell JAD, Vikram DS, van Zijl PCM. Quantitative magnetic susceptibility mapping without phase unwrapping using WASSR. NeuroImage 2014;86:265–279.
32. Nehrke K, Versluis MJ, Webb A, Börnert P. Volumetric B1 + mapping of the brain at 7T using DREAM. Magn Reson Med 2014;71(1):246–256.

SUPPORTING INFORMATION

Additional Supporting Information may be found in the online version of this article.

Fig. S1. Deviations of the fitted WASABI parameters obtained for different SNR between 5 and 50 to the values obtained for optimum SNR. For each data point, 10000 spectra with well-defined SNR were simulated and fitted using Eq. 3. The mean deviations and the standard deviations of the mean deviations are shown for rB_1 (a), $\delta\omega$ (b), parameter *c* (c), and parameter *d* (d). For SNR > 20, the mean deviations of rB_1 and $\delta\omega$ remain unaffected and the standard deviations of the mean deviations are smaller than 0.5% for fitted rB_1 and smaller than 0.5 Hz for fitted $\delta\omega$. The sequence and systems settings are the same as in Figs. 3 and 4.